Materials Science & Engineering C 122 (2021) 111916

Contents lists available at ScienceDirect

Materials Science & Engineering C

journal homepage: www.elsevier.com/locate/msec

Fiber-optic biosensor based on the laccase immobilization on silica-functionalized fluorescent carbon dots for the detection of dopamine and multi-color imaging applications in neuroblastoma cells

Roopkumar Sangubotla, Jongsung Kim *

Department of Chemical and Biological Engineering, Gachon University, 1342 Seongnam Daero, Seongnam-Si, Gyeonggi-Do 13120, Republic of Korea

ARTICLE INFO

Keywords:
Bioprobe
Tapered optical fiber
Dopamine
Detection
Laccase
Multi-color imaging

ABSTRACT

An efficient and cost-effective biosensor is of the great demand for the detection of the biologically significant neurotransmitter dopamine. In this context, enzymatic biosensors show excellent sensitivity and selectivity. In this study, we developed a laccase immobilized fiber-optic biosensor based on the fluorescence principle for the detection of dopamine. To design this biosensor, we used microwave irradiation to synthesize carbon dots (CDs) using curcumin and dimethylformamide, and the resulting CDs were called CDD-CDs. These were functionalized with a silicon precursor, 3-(aminopropyl)-triethoxysilane, and were referred to as APT-CDs. Furthermore, laccase was covalently immobilized to the APT-CDs to construct a novel bioprobe. The CDD-CDs, APT-CDs, and bioprobe showed orange (λ_{em} = 586 nm) green (λ_{em} = 533 nm), and blue-colored emissions (λ_{em} = 476 nm) at 430, 380, and 360 nm excitation wavelengths, respectively. The CDD-CDs and bioprobe showed quantum yields of 14.8% and 10.2%, respectively. The CDD-CDs displayed solvatochromism in various solvents. Bioprobe showed a significant fluorescence quenching for dopamine in the linear range of 0–30 μM with a detection limit of 41.2 nM. Bioprobe was immobilized on the tapered optical fiber using ethyl cellulose by a simple dip-coating method and investigated for multi-color imaging applications. The resulting tapered optical fiber achieved a satisfactory detection limit of 46.4 nM in the dopamine concentration range of 0–10 μM. The bioprobe demonstrated high biocompatibility, long-lasting photostability, and thermal stability, and had sufficient cytotoxicity in human neuroblastoma cells (SH-SY5Y) with excellent multi-color imaging potential. The practicality of the bioprobe was investigated in human serum and cerebrospinal fluid.

1. Introduction

Dopamine (DA) is a clinically significant neurochemical agent that is responsible for various physiological functions throughout the brain. The endogenous concentrations of DA in the human brain are ranging from 10 nM–1 μM. Even, slight variations in the DA levels cause chronic neurodegenerative disorders, such as Parkinson's, Alzheimer's, schizophrenia, and depression [1–5]. Hence, desirable DA sensing strategies are indispensable for early diagnosis and monitoring of these disorders. To date, a myriad of nanomaterials and analytical methods have been proposed for the detection of DA. For instance, Yang et al. have developed dumbbell like FePt-Fe_3O_4 nanoparticles (NPs) for electrochemical sensing of DA and achieved outstanding sensitivity [6]. Liu et al. designed microfluidic paper chips using a colorimetric assay for determining DA in biological samples like serum and plasma [7]. Zhang et al. synthesized 3-mercaptophenylboronic acid (3-MPBA)-modified silver NPs relying on the surface-enhanced Raman spectroscopy (SERS) method [8]. However, these methods are constrained due to the requirement of critical monitoring in the interference of ascorbic acid and uric acid (for electrochemical), comparably low sensitivity (for colorimetry), and complex and expensive laborious setup (for SERS). To address these difficulties, fluorescence methods are appreciable due to their cost-effectiveness, ease of handling, longevity, and surface modification in nanomaterials. Carbon dots (CDs) are versatile zero-dimensional and ultra-nano carbon materials (i.e., size <10 nm) that can replace semiconductor quantum dots (QDs) and fluorescent dyes. The CDs present outstanding features such as hydrophilicity, tunable photoluminescence (PL), and excellent biocompatibility [9–11]. By incorporating these advantages, CDs have been used in multifaceted applications including biosensing, bioimaging, optoelectronics,

* Corresponding author.
E-mail address: jongkim@gachon.ac.kr (J. Kim).

https://doi.org/10.1016/j.msec.2021.111916
Received 9 December 2020; Received in revised form 15 January 2021; Accepted 22 January 2021
Available online 29 January 2021

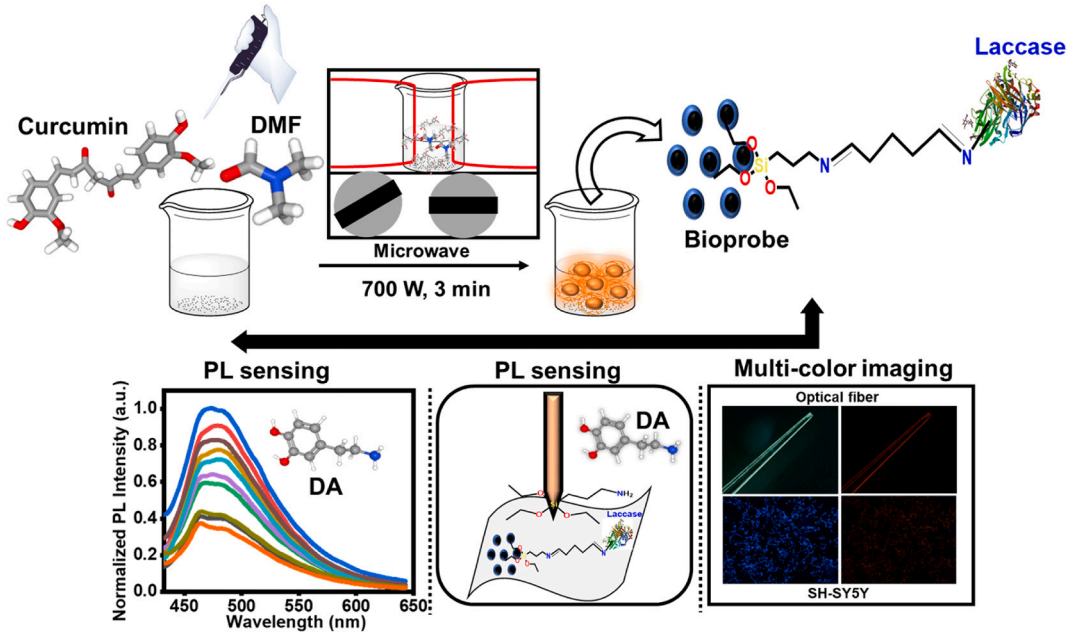

Scheme 1. Schematic illustration of the synthesis of CDD-CDs by microwave irradiation (conditions: 700 W and 3 min) and bioprobe applications for DA sensing and multi-color imaging.

photocatalysis, biolabeling, and drug delivery [12–19]. Specifically, paramount attention has been created in the development of long-wavelength CDs using hydrothermal approaches. These are highly adopted for diverse applications such as bioimaging, in vitro fluorescence sensing, and multi-color LEDs (light emitting diodes) [20–23].

In various biological applications, curcumin, which is widely available as a bioactive material, has versatile benefits. Due to its low aqueous solubility and poor chemical stability, direct synthesis of CDs using curcumin is very challenging. For instance, Pal et al. synthesized multicolor fluorescent CDs by hydrothermal treatment using curcumin and polyethyleneimine (PEI) [18]. More strikingly, curcumin after surface passivation with PEI substantially increased the aqueous solubility of CDs. On the other hand, Lin's group synthesized CQDs by pyrolysis at 180 °C using solid-state curcumin with improved aqueous solubility [24]. Again, the aqueous solubility of CDs depends on the choice of an effective precursor. Dimethylformamide (DMF) tends to be a suitable precursor and organic solvent in this regard due to heteroatom doping and surface passivation properties. In this sense, Gu et al. developed amphiphilic CDs using DMF through hydrothermal treatment for 12 h at 260 °C, which showed high aqueous solubility and biocompatibility [25].

Laccase (EC 1.10.3.2), an enzyme class of oxidase consisting of four copper centers has widely been used for the degradation of contaminants in bioremediation. Mainly this enzyme has been isolated from fungi, bacteria, and other plant parts. In particular, laccase shows a high catalytic performance and sufficient substrate selectivity for phenolic pollutants [26]. Carbon-based materials such as electrospun nanofibers, multi-walled carbon nanotubes (MWCNTs), microporous carbon fibers, graphene-cellulose microfibers, magnetic graphene oxide nanosheets have been reported for immobilizing laccase in a broad biosensor application [27–31]. A plethora of laccase-biosensors already have been developed for DA sensing based on the electrochemical performance. Since the last decade, various functionalized nanomaterials have been utilized to fabricate these sensors such as shape-specific silica-phytic acid NPs, iron oxide and magnetic silica core-shell microspheres, and poly(allylamine hydrochloride) stabilized gold NPs [32–34]. However, these materials require sophisticated synthesis skills with proper operational abilities. Recently, ecofriendly and biocompatible functionalized CDs are highly interested nanomaterials for this purpose. They provide excellent optical properties, magnificent photostability, and chemical stability [35]. In this sense, silica functionalization provides nontoxicity, heteroatom doping, and improved thermal stability to the CDs. Again, it protects CDs from adverse external conditions such as pH, temperature, and salinity. In this case, 3-(aminopropyl)-triethoxysilane (APTES), which is special organosilane, contributes hydrophilicity and amination to CDs for use in biosensors [9]. From the last decade, CDs/enzyme hybrids have been developed for their excellent sensitivity. In this context, Li and Tang groups developed CDs/tyrosinase-based bioprobes for DA detection [36,37]. Both have shown the detection limits up to 60 nM. Again, Shamsipur et al. designed QDs/laccase bioprobe for the determination of DA by capping of thioglycolic acid (TGA) on the CdTe QDs [38]. These bioprobes have shown a detection limit of 0.16 μM. Unfortunately, the above reports lack in vitro studies that indicate the need for more in-depth biological studies using CDs based on enzymes.

Fiber-optic biosensors are favorable for their chemical inertness, cost-effectiveness, flexibility in surface adjustment, and high sensitivity. These sensors have been used to detect biomolecules, bacterial species, and metal ions [39–41]. Moreover, a laccase-coated fiber-optic biosensor was developed by Silva's group to determine the DA [42]. The major limitation, however, involves an advanced experimental set-up. Recently, a wide range of functionalized nanomaterials has been using in the fiber-optic dopamine sensors that are working on the surface plasmon resonance. These include the silver nanoparticles, graphene layer/gold-coated film with DNA aptamers, and Nafion membranes covered with multi-walled carbon nanotubes [43–45]. On the other hand, the optical fibers consist of dense claddings that interrupt the emission of fluorescence. Strict modifications, therefore, need to be made to optical fibers such as grating and tapering [44,46]. Our research group has developed a tapered fiber-optic sensor that worked based on the fluorescence mechanism and tracked brain DA levels [47]. Although the sensors were cost-effective and sensitive, biocompatibility remains a challenge due to the highly toxic nature of the semiconductor QDs. In view of these aspects, we have synthesized biocompatible CDD-CDs using curcumin and DMF by microwave irradiation. The CDD-CDs showed solvatochromism and excitation-independent PL emission properties in different solvents. Subsequently, the CDD-CDs were functionalized with APTES, which allowed the design of a novel bioprobe through laccase immobilization. In addition, the bioprobe was used to

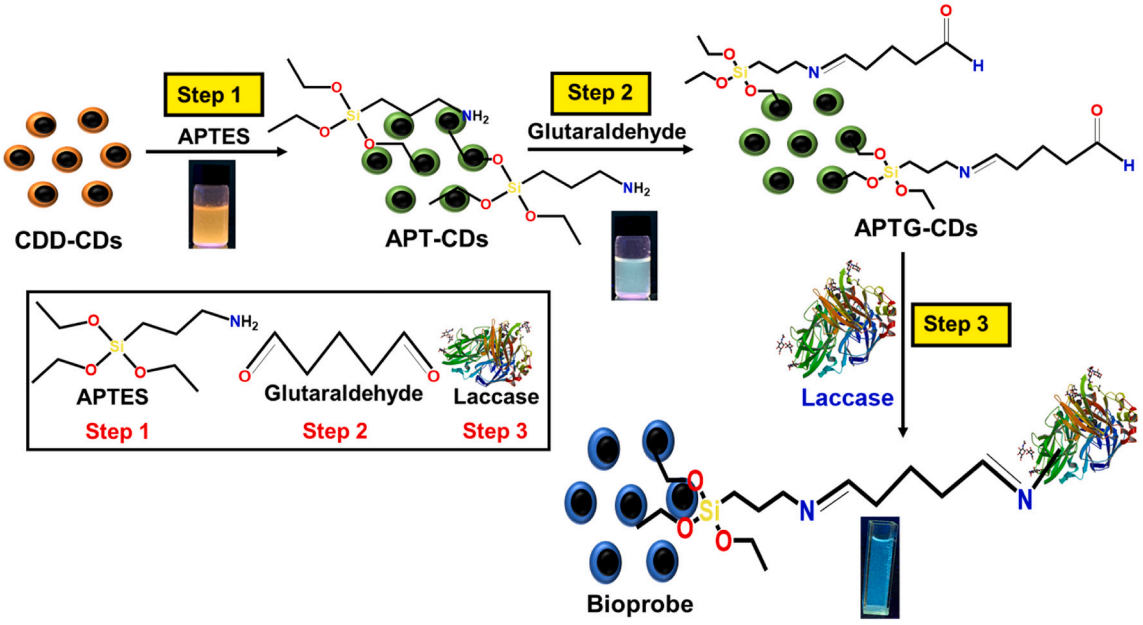

Scheme 2. Schematic illustration for the silica-functionalization of CDD-CDs and laccase enzyme immobilization on CDD-CDs.

detect DA with optimum selectivity and sensitivity. Bioprobes were used to detect DA in real samples, including human serum and cerebrospinal fluid (CSF).

2. Experimental

2.1. Synthesis and purification of CDD-CDs

The CDD-CDs were synthesized by microwave irradiation, using curcumin and DMF as the precursor and solvent, respectively. All glassware was cleaned using aqua regia ($HCl:HNO_3$ = 3:1, v/v) before the experiment. In a typical synthesis, 60 mg of curcumin powder was dissolved in 45 mL of DMF and thoroughly mixed to form a homogeneous solution in a beaker. This solution was heated in a microwave oven (700 W) for 3 min. After the reaction, the color of the solution was changed to wine red, which indicated CDD-CDs formation (Scheme 1). Then, the solution was cooled to room temperature, washed three times with deionized (DI) water, and centrifuged (9000 rpm, 20 min). Further, CDD-CDs were purified by dialysis against DI water for 24 h using a cellulose ester membrane (molecular weight cutoff: 2 kDa) to remove unreacted curcumin moieties and DMF. The dialyzed solution was filtered using a 0.22-μm syringe filter, and finally, CDD-CDs were obtained by rotary evaporation. The dried CDD-CDs were appeared as the brick-red powder (Fig. S1 a).

2.2. Laccase immobilization on CDD-CDs

We immobilized laccase on CDD-CDs using both physical and chemical methods. The physical method included the adsorption of laccase on CDD-CDs following the reported method [26]. First, 100 mg of CDD-CDs was mixed with 200 mg of laccase in 200 mL citrate-phosphate buffer (pH 5.2). This mixture was placed in a shaking incubator at 120 rpm and 30 °C for 4 h to maintain adsorption equilibrium. Then, the mixture was centrifuged (8000 rpm, 5 min) and washed thrice

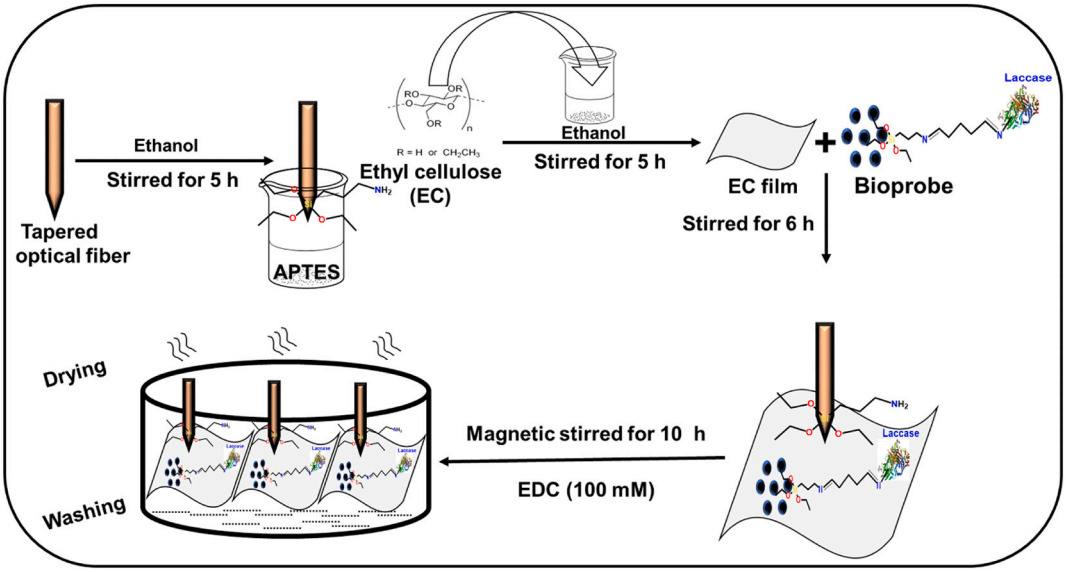

Fig. 1. Schematic representation for the immobilization of bioprobe over the tapered optical fiber using ethyl cellulose (EC) coating.

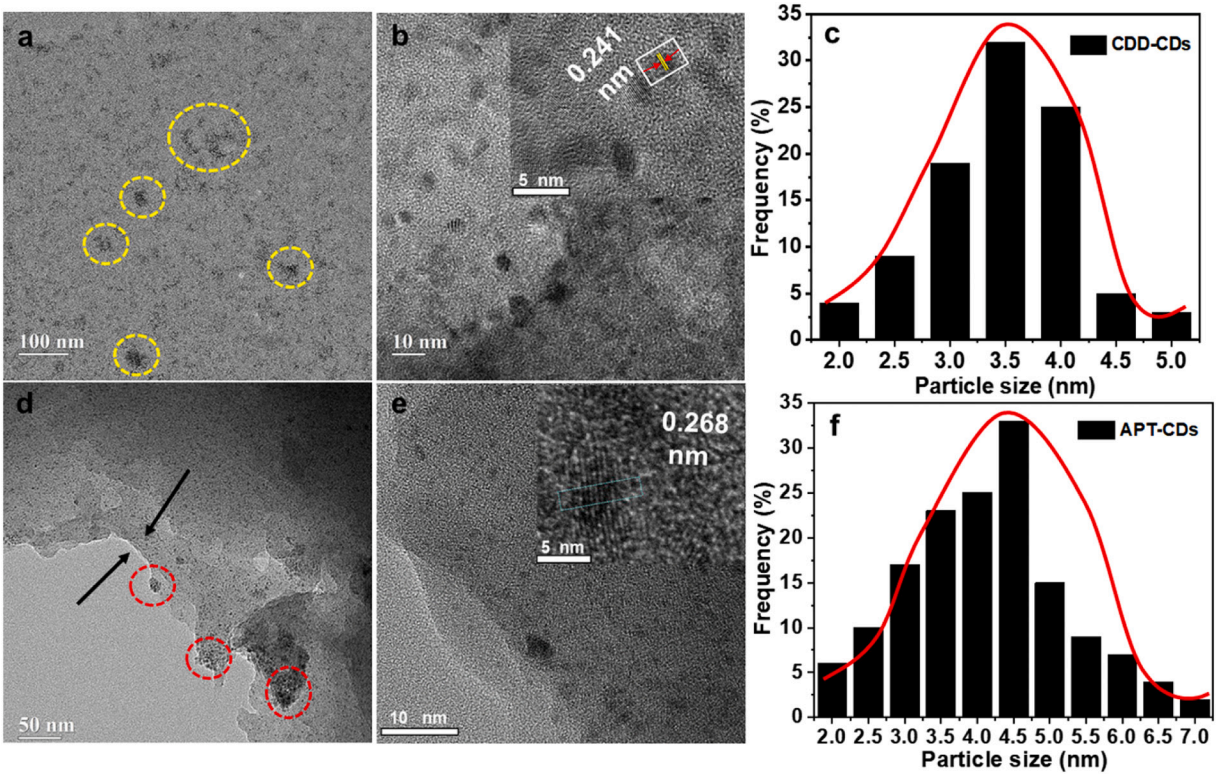

Fig. 2. TEM and HRTEM images of (a, b) CDD-CDs and (d, e) APT-CDs, respectively (inset of (b, e) represents their lattice spacings) and Gaussian particle size distribution curves of (c) CDD-CDs and (f) APT-CDs, respectively. (For interpretation of the references to color in this figure, the reader is referred to the web version of this article.)

with citrate-phosphate buffer to remove free or unbound laccase. This sample was freeze-dried and stored in a refrigerator for further experiments. The chemical method included a covalent immobilization with little modification of the previous methods [44,48]. The overall process is described in three steps, as illustrated in Scheme 2. The CDD-CDs were aminated and stabilized using APTES. A homogeneous solution of CDD-CDs in ethanol (1 mg mL^{-1}) was prepared in an ultrasonic bath for 30 min. Then, APTES (0.2 mL) was added to the solution containing CDD-CDs under continuous agitation for 72 h. The solution was termed APT-CDs and thoroughly washed with DI water and vacuum dried. Then, APT-CDs were placed in a 50 mL beaker containing 10 mL glutaraldehyde (GA) (5% v/v) and stirred for 12 h at room temperature and the resulting solution was named as APTG-CDs (Step 2). During this procedure, enough aldehyde groups were produced on the surface of APTG-CDs. Immediately, APTG-CDs were thoroughly rinsed using phosphate-buffered saline (PBS, 10 mM, pH 7.4) and DI water to remove excess GA groups on the APTG-CDs. Then, 15 mL of laccase solution (1 mg mL^{-1} in PBS, 10 mM, pH 7.4) was added to the APTG-CDs in a beaker (Step 3). This mixture was kept in an ice-water bath with continuous stirring at 25 °C for 24 h. Later, this mixture was washed with PBS (10 mM, pH 7.4) and DI water. Finally, this mixture was vacuum dried and a colorless powder (i.e., bioprobe) was formed (Fig. S1 b). The resultant bioprobe was refrigerated at 4 °C for further experiments.

2.3. Tapered optical fiber preparation

The optical fibers were tapered according to the earlier method [47]. First, optical fiber tips were dipped in conc. H_2SO_4 at 100 °C to remove the polyimide coat. Immediately after, tips were cleansed with DI water, dipped in HF using a syringe pump, and finally air-dried.

2.4. Bioprobe immobilization on the tapered optical fiber

The immobilization of bioprobe on the tapered optical fiber was carried out by adopting slight modifications to the former method [49]. The optical fiber tips were thoroughly washed with water and immersed in 10% (v/v) APTES in ethanol for 5 h at room temperature (Fig. 1). Next, the fiber tips were washed with DI water and ethanol to remove unreacted amine groups from the APTES. Finally, all the amino-functionalized fiber tips were dried in a hot air oven at 80 °C for 20 min. The free amine groups that formed on the fiber tip surface bound to the carboxylic group on the surface of the bioprobe. The amino-functionalized fiber tips were immobilized by bioprobe using the dip-coating method. Ethyl cellulose (EC) was used as a thickening agent (0.2 g) dissolved in ethanol (5 mL) and stirred for 5 h, which resulted in the formation of an EC film. Then, 1 mL of bioprobe was added to the EC film and continuously stirred for 6 h at room temperature. Fiber tips (diameter, 600 μm) were coated with the EC film using the dip-coating process. Further, the immobilized optical fiber tips were immersed in the EDC (100 mM) continuously, under magnetic stirring for 10 h. Later, all optical fiber tips were immediately washed with water and air-dried for 20 min.

2.5. Dopamine detection using bioprobe

The bioprobe was employed for DA detection using fluorescence sensing. In a typical run, 100 μL of bioprobe was added to a cuvette that contained 2 mL of PBS (10 mM, pH 7.4). Different concentrations of DA (0–30 μM) were added to the above reaction mixture and incubated for 30 min. Finally, all fluorescence spectra were recorded using a PL spectrophotometer at an optimal temperature of 25 °C.

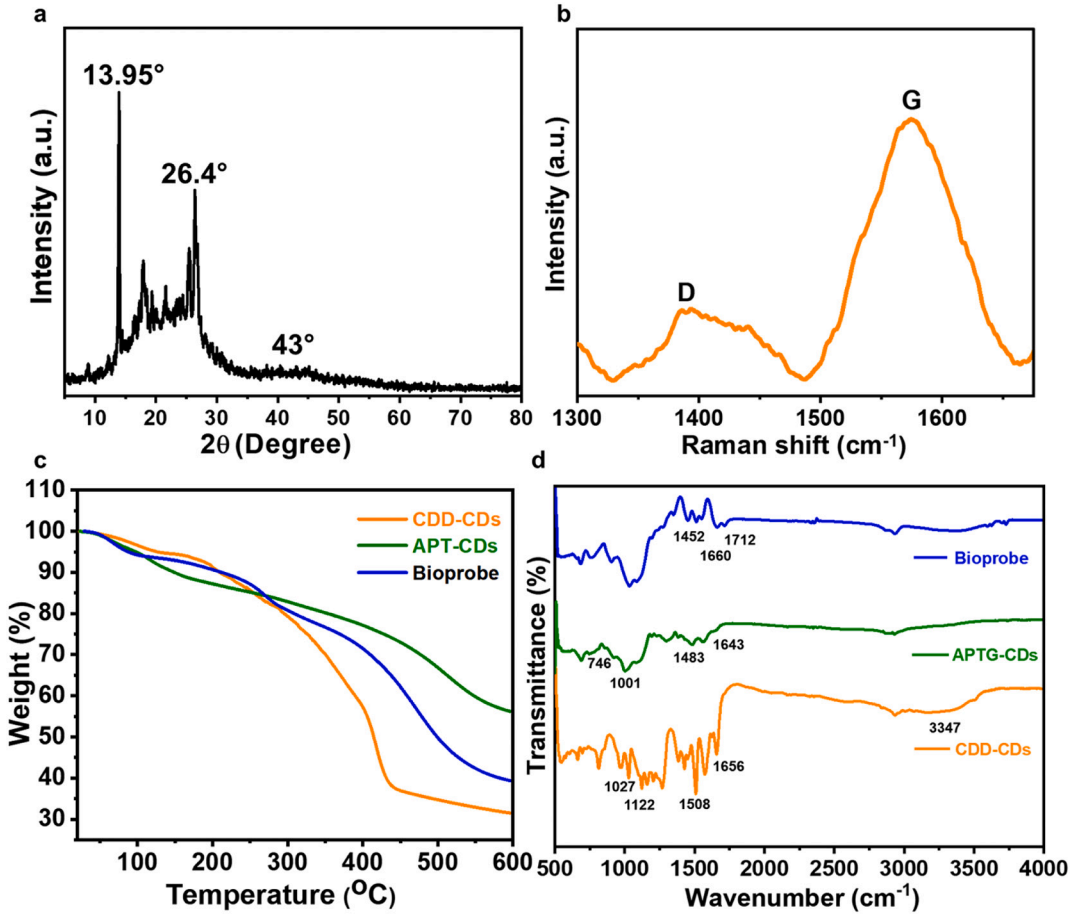

Fig. 3. (a) XRD pattern of the CDD-CDs. (b) Raman spectrum of the CDD-CDs. (c) TGA analysis of the CDD-CDs (orange curve), APT-CDs (green curve), and bioprobe (blue curve), and (d) FT-IR spectra of the CDD-CDs (orange line), APTG-CDs (green line), and bioprobe (blue line). (For interpretation of the references to color in this figure legend, the reader is referred to the web version of this article.)

2.6. Cell culture

Human neuroblastoma cell lines (SH-SY5Y) were cultured according to the instructions provided by the American Type Culture Collection using Dulbecco's Minimum Essential Medium and 15% fetal bovine serum (FBS) with 1% penicillin-streptomycin. The cells were incubated at 37 °C in a 5% CO_2 atmosphere and sub-cultured until 80–90% confluence was achieved.

2.7. Cell proliferation (MTT) assay

In a six-well plate, SH-SY5Y cells were cultured and incubated for 24 h at 37 °C and 5% CO_2, up to 80–90% confluency. The medium was then thoroughly discarded and combined the fresh medium with various concentrations of bioprobe from 20, 40, 60, 80, 100, and 120 μg mL^{-1}, and incubated for the next 48 h. The medium was replaced with the MTT reagent after incubation and the cells were incubated for 3 h with the reagent. Further, through a microplate reader, the absorbance was recorded at 570 nm.

2.8. Multi-color imaging studies of SH-SY5Y cells and tapered optical fibers using bioprobe

SH-SY5Y cells were seeded in an essential medium in a six-well plate with coverslips and incubated for 24 h with 5% CO_2 at 37 °C. Immediately after incubation, the medium was removed, and the cells were washed with Dulbecco's phosphate-buffered saline (DPBS), to remove the remaining medium. SH-SY5Y cells were incubated in 5% CO_2 at 37 °C for 3 h with bioprobe. Then, the coverslips were washed three times with DPBS, and the fluorescence microscope was used to obtain the corresponding cell images.

The tapered optical fibers were thoroughly cleaned with DI water and maintained throughout the experiment. A freshly prepared bioprobe was immobilized on the tips of the tapered optical fibers. Then, these were incubated for 3 h in dark conditions at room temperature in advance for imaging studies. Finally, these tips were cautiously fixed on the microscopic slide, and images were acquired through the fluorescence microscope.

2.9. Statistical analysis

All the results in this report are represented as the mean and standard deviation (±SD) of three individual experiments.

3. Results and discussion

3.1. Materials characterization

The structural properties of the CDD-CDs and APT-CDs were characterized using transmission electron microscopy (TEM), high-resolution TEM (HRTEM), scanning electron microscopy (SEM), and X-ray diffraction (XRD). Fig. 2 a (yellow circles) and Fig. 2 b show the TEM and HRTEM images of CDD-CDs, respectively, which reveal that they are spherical and well dispersed, without any aggregation. The inset in Fig. 2 b shows portions that present a well-resolved lattice spacing of 0.241 nm, which suggests that the CDD-CDs are mainly

crystalline, while other portions have an amorphous structure. These HRTEM results are consistent with the XRD results. Fig. 2 d (red circles) and Fig. 2 e show the TEM and HRTEM images of APT-CDs, respectively, where the silicon layer covers most of the APT-CDs, as indicated by the arrows. Further, this image shows that the particles are spherical and uniformly dispersed. The inset image shows that the particles are mostly amorphous, and some weakly crystalline portions with 0.268 nm lattice spacing. Fig. 2 c and f show the Gaussian fitting curves for the CDD-CDs and APT-CDs, with sizes of 2–5 and 2–7 nm, respectively. The powder XRD plot (Fig. 3 a) of the CDD-CDs shows distinct sharp peaks at 13.95° and 26.4°, which signifies the disordered carbon atoms and crystalline nature, and a broad peak at 43°, which suggests that some portions of CDD-CDs are amorphous. To investigate the detailed structural changes, we carried out XRD studies for APT-CDs and bioprobe. The XRD pattern of APT-CDs showed a moderately broad peak at 21.34°, which is attributed to the (002) plane with the graphitic structure (red line, Fig. S2 a). This may also be attributed to the formation of amorphous siloxane moieties on the CDD-CD surface [50]. These XRD results correlated with the HRTEM results that were observed for APT-CDs. Further, the XRD pattern of the bioprobe showed a typical broad peak around 23.91°, which is assigned to the (002) plane with the graphitic structure. This broadened bioprobe peak suggests that amorphous siloxane groups were adequately formed [51]. In addition, intense sharp and very weak diffraction peaks are observed around 31.65° and 45.3°, which correspond to the (110) and (111) lattice planes, respectively (blue line, Fig. S2 a). This suggests that the functionalized bioprobe preserves the crystalline nature, as observed in CDD-CDs. Further, the XRD pattern of the physically immobilized CDD-CDs shows a broad (002) diffraction peak around 28.8°, which suggests an amorphous nature with highly disordered carbon atoms (Fig. S2 b). These results are well correlated with the reported literature [52–54].

Raman spectra were obtained to investigate the defects and graphitization of CDD-CDs, as shown in Fig. 3 b. The peaks at 1385 and 1575 cm^{-1} are assigned to the D and G bands, respectively. The D band at 1385 cm^{-1} corresponds to disorders or defects of sp^3 carbons or surface states on the CDD-CDs. The G band at 1575 cm^{-1} corresponds to sp^2 carbons that were present on the surface of CDD-CDs. The high G/D intensity ratio (I_G/I_D) indicates a high-quality graphitic structure [55]. These results are consistent with the HRTEM results and confirm the crystalline graphitic structure of the CDD-CDs.

To examine the thermal stability of CDD-CDs, APT-CDs, and bioprobe, we performed the thermogravimetric analysis (TGA). Thermal decomposition of CDD-CDs (orange curve) has occurred at different temperatures (from 20 to 600 °C) in four phases, as shown in Fig. 3 c. The initial weight loss, which is responsible for the loss of water molecules and hydroxyl (O—H) groups on the surface, was observed between 20 and 142.92 °C (5.416%). The second weight loss occurred between 142.92 and 391.10 °C (34.89%). It is due to the decomposition of functional groups dependent on oxygen and nitrogen, such as (C═O) and (C—N). The third and final weight losses were observed between 391.10 and 454.66 °C (22.98%) and 454.66 and 600 °C (5.206%) due to the degradation of aliphatic (C—C) and aromatic (C═C) groups.

Additionally, the thermal decomposition of APT-CDs and bioprobe occurred in three stages. In the first stage, APT-CDs (green curve) showed weight loss below 100.55 °C (5.661%), which is due to the escape of moisture or O—H groups. In the second stage, weight loss was observed below 234.32 °C (8.702%), which is attributed to the decomposition of functional groups, such as nitrogen-based (C—N, C═N, and −NH2) and oxygen-containing [(C═O) and (C—O)] groups. The final weight loss was observed between 234.32 and 600 °C (29.62%). Since the APTES boiling point is approximately 217 °C, all the physically attached APTES groups may have decomposed below 300 °C. The remaining chemically bonded APTES groups decomposed at 500 °C. Again, the C—Si groups may have degraded from APT-CDs above 450 °C [56]. The bioprobe (blue curve) shows an initial weight loss below 119.31 °C (6.447%), which was responsible for the removal of physically adsorbed water content and −OH groups. In the second stage below 335.41 °C (16.28%), the weight loss is due to the decomposition of C—N, C═N, and COO^- functional groups. The final weight loss occurred between 335.41 and 600 °C (38.11%), which is due to the degradation of physically adsorbed and chemically bonded APTES groups in the bioprobe. The total weight losses for the CDD-CDs, APT-CDs, and bioprobe were 68.49, 43.99, and 60.85%, respectively. It implies that silica-functionalized CDs (i.e., APT-CDs) have outstanding properties of thermal stability and add superior thermal stability to enzyme-bound APT-CDs (i.e., bioprobe). We assume that these advantages facilitate the silicon-functionalization of nanomaterials for the design of enzyme-based biosensors. Table S1 determines the average temperature ranges and their corresponding weight loss percentages for the above materials.

Elemental analysis was performed using SEM-EDX for the APT-CDs and bioprobe, to understand silicon-functionalization and enzyme immobilization. Fig. S3 a–d shows the elemental mapping of the APT-CDs, which identify elements such as carbon (C), oxygen (O), silicon (Si), and nitrogen (N). Fig. S3 e shows the SEM image of the APT-CDs. Elemental mapping of the bioprobe shows elements such as carbon (C), oxygen (O), silicon (Si), chlorine (Cl), phosphorous (P), nitrogen (N), sodium (Na), and potassium (K), and the corresponding SEM image is illustrated in Fig. S4 a–i. Also, the EDX spectra of APT-CDs and bioprobe are shown in Figs. S5 and S6, which demonstrates that APTES and laccase are well-functionalized on the CDD-CD surface.

Fourier-transform infrared (FT-IR) spectroscopy was employed to investigate the functional groups present on the CDD-CDs, APTG-CDs, and bioprobe (Fig. 3 d). The CDD-CDs demonstrate typical peaks at 1027, 1122, 1508, 1656, and 3347 cm^{-1} that represent the stretching vibrations of (C—O), (C—N), aromatic (C═C), (C═O), and (O—H) groups, respectively (orange line) [57]. After the functionalization of CDD-CDs with APTES, the FT-IR spectra of APTG-CDs show peaks at 746, 1001, 1483, and 1643 cm^{-1}, which represent the stretching vibrations of (Si—O—C), (asymmetric, Si—O—Si), (C═N), and (C═O) functional groups, respectively (green line) [58,59]. The presence of Si-containing functional groups and stretching vibrations of $-CH_2$ and $-CH_3$ groups suggest the functionalization reaction between the CDD-CDs and APTES. The symmetric and asymmetric stretching vibrations of $-CH_2$ and $-CH_3$ groups were observed at 2842 and 2931 cm^{-1} and 2883 and 2987 cm^{-1}, respectively, as shown in the magnified portion of Fig. S7 a [9]. The appearance of the C═N stretching vibrations confirmed the reaction between the GA aldehyde group and the APT-CDs amine groups. The FT-IR spectra of the bioprobe demonstrated a typical amide I band (due to the C═O stretching vibration) and an amide II band (due to N—H bending and C—N stretching vibrations) at 1660 and 1552 cm^{-1}, respectively. The presence of these bands confirms laccase immobilization on the CDD-CDs [60]. The bioprobe also showed COO^- and −OH group stretching vibrations at 1712 and 3394 cm^{-1}, respectively. The COO^- stretching vibrations may be attributed to the free or unreacted GA aldehyde groups or laccase enzyme carboxylic acid groups after immobilization. After immobilization of APTG-CDs with laccase enzyme, the FT-IR spectra of the bioprobe showed peaks at 2869 and 2933 cm^{-1}, which correspond to the symmetric $-CH_3$ and asymmetric $-CH_2$ stretching vibrations that originated from APTES. The presence of C═N stretching vibrations at 1452 cm^{-1} supports the reaction between the GA aldehyde groups and the laccase enzyme amine groups (blue line). The bioprobe FT-IR spectra show alkyl group stretching vibrations at 2869 and 2933 cm^{-1}, which are attributed to the $-CH_3$ symmetric and $-CH_2$ asymmetric stretching vibrations, respectively, as illustrated in the magnified portion of Fig. S7 b. The occurrence of these stretching vibrations suggests the incorporation of laccase enzymes into APTCDs. Further, FT-IR spectra of the physically immobilized bioprobe are illustrated in Fig. S7 c. The peaks at 1265, 1581, and 1705 cm^{-1} are attributed to the stretching vibrations of the (C—N), aromatic (C═C), and (COO^-) groups, respectively. The O—H stretching vibrations at 3255, 3347, and 3595 cm^{-1} of the bioprobe are due to the

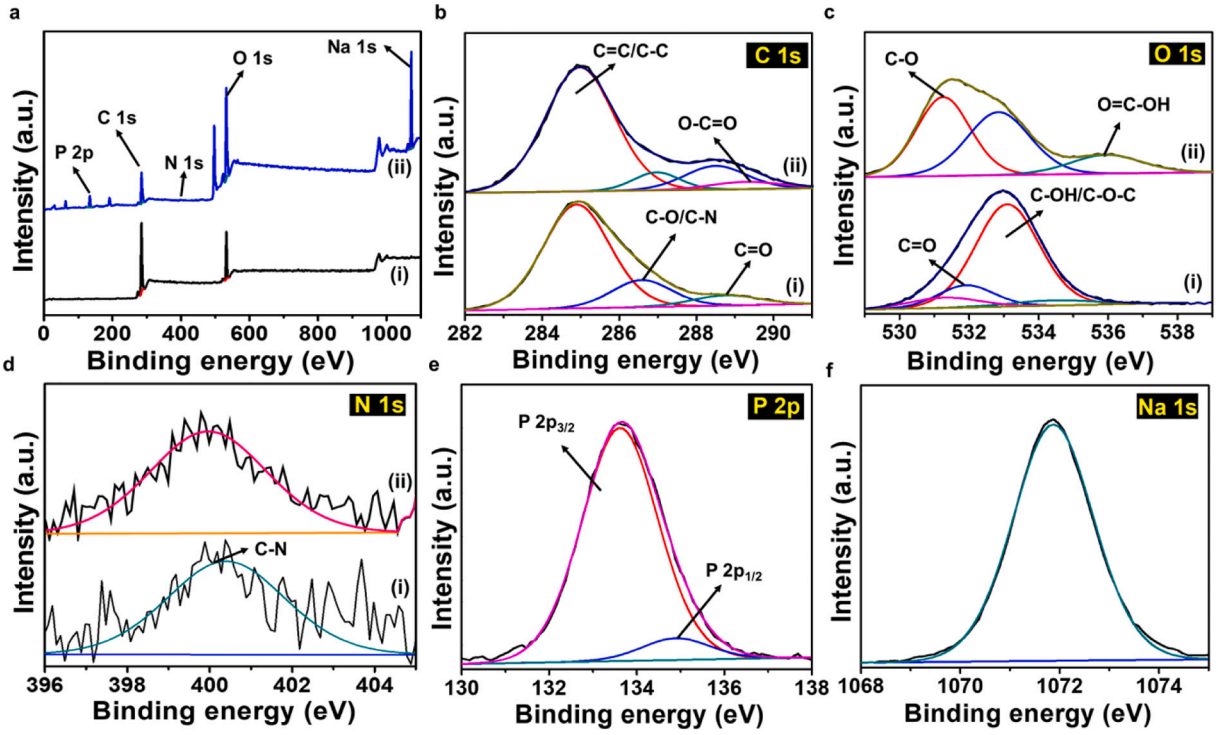

Fig. 4. (a) XPS survey spectra of (i) CDD-CDs (ii) physically immobilized bioprobe, (b–f) high-resolution spectra of C 1s, O1s, N 1s, P 2p, and Na 1s.

curcumin precursor and laccase enzyme incorporation.

The elemental composition and chemical environments of the CDD-CDs after physical and chemical immobilization were investigated using XPS studies. The CDD-CDs were mainly composed of C 1s, O 1s, and N 1s. After physical immobilization of the CDD-CDs with laccase enzyme, the XPS total survey spectrum reveals additional elements, such as P 2p and Na 1s (Fig. 4 a). The high-resolution spectra of C 1s reveal three peaks at 284.9, 286.58, and 288.77 eV, which are attributed to C═C/C—C (sp^2 and sp^3), C—O/C—N, and C═O, respectively (Fig. 4 b) [61]. Interestingly, another peak was observed in the immobilized CDD-CDs at 289.27 eV that corresponds to O—C═O. Fig. 4 c shows the O 1s high-resolution spectra of CDD-CDs, which demonstrate deconvolutions at 531.3, 531.92, and 533.1 eV that correspond to C—O, C═O, and C—OH/C—O—C, respectively. An additional peak was observed at 535.91 eV, which was attributed to O═C–OH in the physically immobilized CDD-CDs. From the high-resolution spectra of C 1s and O 1s, the O—C═O group was observed in the physically immobilized CDD-CDs, and this agrees well with the FT-IR results. The high-resolution spectra of N 1s for the CDD-CDs before and after physical immobilization demonstrated a single peak, at 400.39 and 399.95 eV, which corresponds to C—N (Fig. 4 d). Notably, the CDD-CDs after physical immobilization showed two elements, P 2p and Na 1s, in the high-resolution XPS. The high-resolution P 2p spectrum showed two peaks, at 133.62 and 134.89 eV, which are attributed to P $2p_{3/2}$ and P $2p_{1/2}$, respectively (Fig. 4 e). A single peak was observed at 1071.87 eV in the high-resolution Na 1s spectrum (Fig. 4 f). The presence of these elements is due to the addition of phosphate-citric buffer during the physical adsorption process.

Further XPS analysis was performed to understand the covalent immobilization process between APTG-CDs and the bioprobe. The XPS total survey spectrum of APTG-CDs showed the presence of elements such as C 1s, O 1s, N 1s, and Si 2p. The peaks for the above elements were identified at approximately 284.82, 532.13, 399.29, and 102.25 eV, respectively (Fig. 5 a). The high-resolution C 1s spectra show three peaks, at 284.93, 286.72, and 288.66 eV, which are attributed to C—C/C—H, C—O/C—N, and C═N/C═O, respectively (Fig. 5 b). Fig. 5 c shows the O 1s high-resolution APTG-CDs spectra, which exhibited three peaks, at 530.97, 532.47, and 533.86, which were responsible for C—O/Si—O, C═O/Si—O—Si, and Si—O—C, respectively [62]. The appearance of organic and inorganic silicon functional groups suggests that CDD-CDs have successfully participated in the silicon-functionalization process. Also, the O 1s high-resolution spectra of the bioprobe revealed one more peak at 535.47 eV, which has attributed to O═C–OH [63]. These results have well supported FT-IR observations. The high-resolution N 1s spectra for the APTG-CDs show three peaks, at 397.43, 399.42, and 401.05 eV, which are attributed to C═N—C, (O═C—NH/C—NH), and N—C_3, respectively (Fig. 5 d) [64]. The appearance of C═N in the high-resolution C 1s and N 1s spectra from APTG-CDs suggested that APT-CDs amino groups were successfully functionalized with GA aldehyde groups, as shown in step 2. Again, free aldehyde groups present in the APTG-CDs were readily attached to the amino groups of the laccase enzyme (step 3). The high-resolution Si 2p spectra for the APTG-CDs were present at 102.63, which may be attributed to the organic and inorganic silicon groups, i.e., Si—O—C and Si—O—Si (Fig. 5 e) [65]. This indicates that the APT-CDs were modified through APTES, and these silicon groups were further distributed on the bioprobe surface. In addition, a peak at 1072.49 eV was observed in the high-resolution Na 1s spectrum from the bioprobe (Fig. 5 f). It may have resulted in the PBS buffer treatment at the time of chemical immobilization. The peaks with similar chemical bonding and their slight shifting suggest successful covalent immobilization between APTG-CDs and the bioprobe. All the FT-IR and XPS results are well consistent and proved covalent immobilization that is used in this study to design the bioprobe as state of the art.

3.2. Optical properties

The optical properties of the CDD-CDs, APT-CDs, and bioprobe were investigated using UV–Vis and PL spectroscopy techniques. Fig. S8 a (orange curve) shows the UV–Vis absorption spectra of the CDD-CDs, with two absorption bands at 225 and 426 nm, which are assigned to the π-π* (mainly aromatic sp^2 domains from curcumin) and n-π* (due to

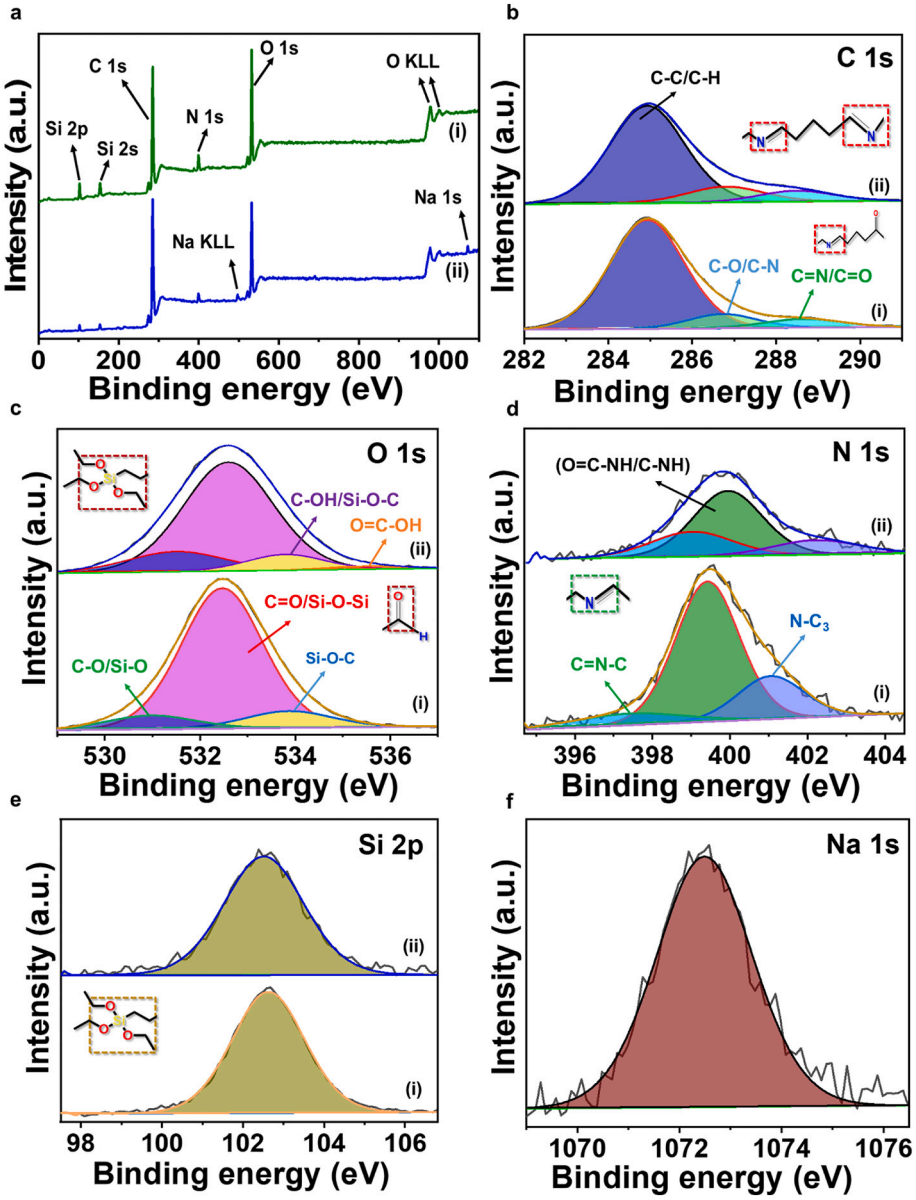

Fig. 5. (a) XPS survey spectra of (i) APTG-CDs (ii) bioprobe, (b–f) high-resolution spectra of C 1s, O1s, N 1s, Si 2p, and Na 1s.

functional groups on the CDD-CDs surfaces) transitions, respectively. After the chemical modification of CDD-CDs with APTES (i.e., APT-CDs), five absorption bands were observed at 205, 248, 286, 348, and 419 nm, as shown in Fig. S8 a (green curve). The first three absorption bands are attributed to the π-π* (aromatic sp^2 domains), and the remaining two are responsible for the n-π* transitions of C═O and other functional groups formed on the APT-CDs surfaces. The strong UV absorption band at 426 nm in the CDD-CDs was blue-shifted to 419 nm, and an additional absorption band was formed at 348 nm, in the APT-CDs. Fig. S8 b shows the PL emission maximum of the CDD-CDs at 586 nm under excitation wavelength of 430 nm. Again, PL emission maximum of APT-CDs was blue-shifted (~53 nm) from 586 to 533 nm at excitation wavelength of 380 nm, as illustrated in Fig. S8 c. The shifting of the absorption and emission spectra and the evolution of green emission in these CDs have attributed to the silica-functionalization (i.e., APTES) of CDD-CDs [9]. The formation of different silicon functional groups on the surface of APT-CDs may be responsible for the change in optical properties. Again, the UV absorption from the bioprobe revealed a single absorption band at 234 nm, which corresponds to the π-π* transition, as shown in Fig. S8 a (blue curve). Two additional absorption bands were completely diminished, at 296 and 416 nm in the bioprobe, due to the incorporation of laccase enzyme on the APT-CDs. The PL emission maximum of bioprobe was blue-shifted (~57 nm), from 533 to 476 nm, at excitation wavelength of 360 nm, as shown in Fig. S8 d. The insets from Fig. S8 b–d show the corresponding emission colors of the CDD-CDs (orange), APT-CDs (green), and bioprobe (blue) under UV light, respectively.

3.3. Solvatochromism of CDD-CDs

The CDD-CDs exhibited solvent polarity-dependent PL emission behavior in various solvents. For this, 13 solvents were chosen based on their polarity (lowest to highest polarity), and the corresponding UV–Vis absorbance and PL emission characteristics were thoroughly investigated. The CDD-CDs demonstrated a bathochromic shift in the PL emission maxima (λ_{max}), from 499 to 562 nm, when observed under a single excitation wavelength (Fig. 6 a). This enables the fluorescence color to change from cyan to light orange, as illustrated in Fig. 6 c. This shift in λ_{max} of the CDD-CDs preferentially depends on the relative polarity parameter (E_T^N) of the solvents, as listed in Table S2. The UV–Vis absorbance spectra of the CDD-CDs dispersed in the above solvents

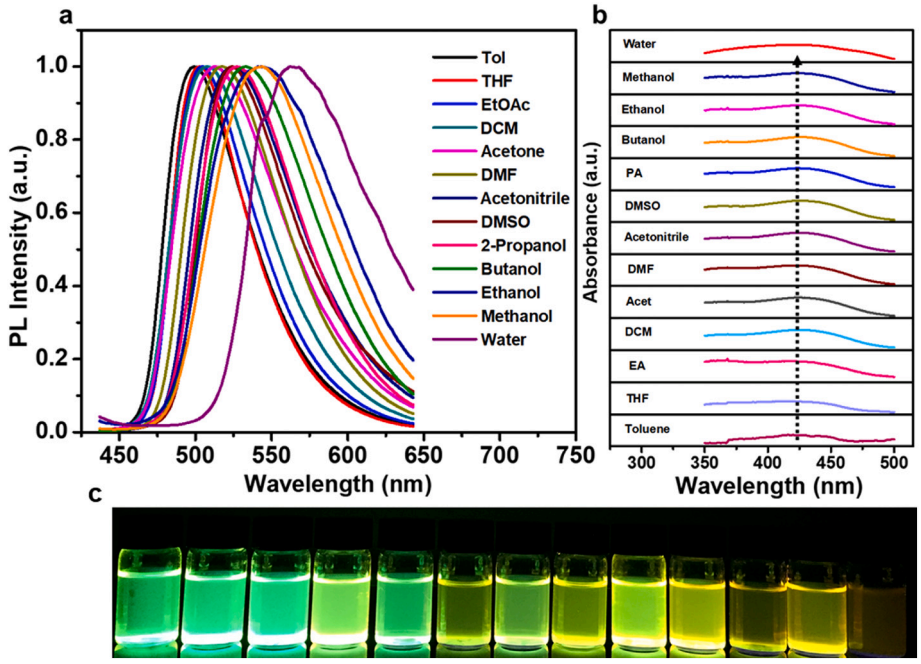

Fig. 6. (a) Normalized PL emission spectra. (b) UV–Vis absorption spectra, and (c) corresponding photographs of CDD-CDs in different solvents based on their polarity showing fluorescence color change from cyan to light orange under UV–Vis light. (For interpretation of the references to color in this figure legend, the reader is referred to the web version of this article.)

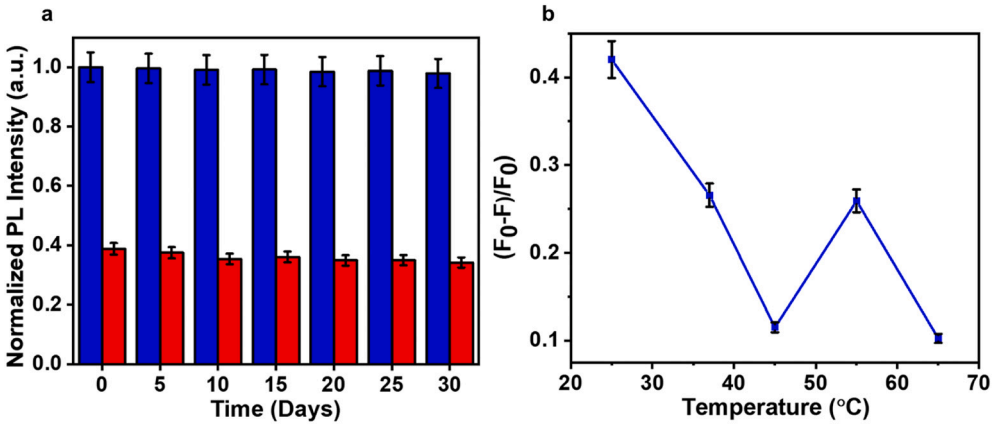

Fig. 7. (a) Fluorescence stability of the bioprobe over a month (five-day interval) without (blue bar) and with (red bar) treatment of DA (30 μM), and (b) the fluorescence quenching efficiency of the bioprobe after the addition of DA (30 μM) at various temperatures (25–65 °C). (For interpretation of the references to color in this figure legend, the reader is referred to the web version of this article.)

exhibited an almost blue-shift, except in water, as shown in Fig. 6 b. This red-shift of the absorbance spectra in water may be attributed to the low aqueous solubility of the CDD-CDs. The UV–Vis absorbance bands of the CDD-CDs were centered at 416, 417, 419, 423, 424, 427, 425, 430, 434, 432, 433, and 419 nm, respectively, in various solvents such as toluene, THF, EA, DCM, acetone, DMF, acetonitrile, DMSO, propanol, butanol, ethanol, methanol, and water, respectively. These results suggest that the CDD-CDs consisted of different surface states in different solvents. Further, we investigated the emission behavior of the CDD-CDs in the abovementioned solvents at different excitation wavelengths. We found that the CDD-CDs exhibited excitation-independent emission properties in each of the solvents, as shown in Fig. S9. It is already known that the surface states of the CDD-CDs play a dominant role in this behavior with regards to preferred morphological characteristics [66].

3.4. Fluorescence sensing of DA using bioprobe

As shown in Fig. 7 a, the bioprobe showed high fluorescence stability over a month when it was stored separately from and along with DA (30 μM). Its stable fluorescence emission suggests that the bioprobe shows promising biosensing and bioimaging applications. Furthermore, the fluorescence quenching efficiency of the bioprobe was examined after the addition of DA (30 μM) at different temperatures (Fig. 7 b). The optimal fluorescence quenching efficiency was observed for the bioprobe at 25 °C, which may be due to the catalytic activity of the laccase enzyme. Hence, we conducted a sensing experiment at 25 °C. The sensitivity of the bioprobe was explored by measuring the PL intensity at different concentrations of DA. The PL intensity of bioprobe gradually decreased after adding DA of various concentrations from to 0–30 μM, as illustrated in Fig. 8 a. Furthermore, a linear regression curve was plotted between ($F_0 - F / F_0$) and DA concentrations (0–0.4 μM) and presented a

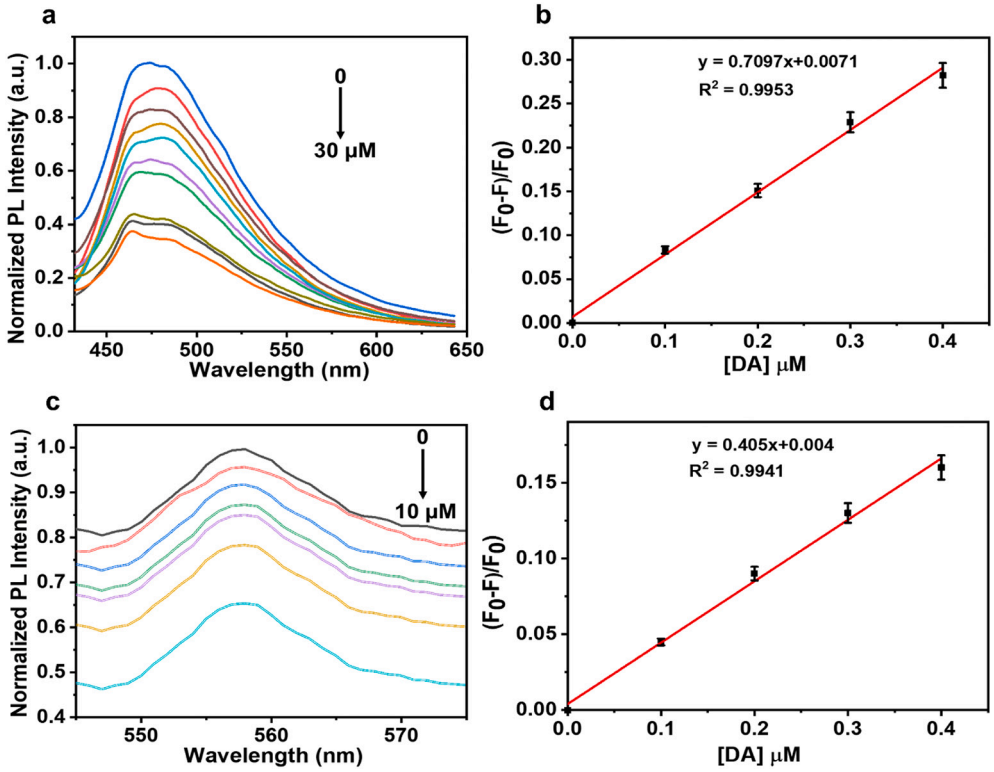

Fig. 8. (a) PL emission spectra of the bioprobe after the addition of various DA concentrations (0–30 μM). (b) Linear plot between (F_0 – F / F_0) and DA concentrations. (c) PL emission spectra of the bioprobe after immobilization on the optical fiber (DA concentrations from 0 to 10 μM), and (d) Linear relationship between (F_0 – F / F_0) and DA concentrations.

good correlation coefficient (R^2 = 0.995) (Fig. 8 b). The limit of detection (LOD) for DA was calculated to be 41.2 nM as per the 3σ/K. Both σ and K indicate the standard deviation and slope of the regression curve, respectively [67]. As mentioned earlier, DA concentrations in the human brain are approximately up to 1 μM [5]. On contrary, similar bioprobes that designed before having demonstrated comparatively less sensitivity than our bioprobe towards DA sensing [36–38]. Based on these facts, our results suggest that the proposed bioprobe has adequate sensitivity for the determination of DA.

In addition, PL measurements were performed on the physically immobilized bioprobe, which exhibited maximum PL excitation and emission of 390 and 550 nm, respectively, as shown in Fig. S10 a. The inset shows light yellow-color emission under UV–Vis light. In addition, sensitivity parameters were compared between the physically and chemically immobilized bioprobes by measuring the fluorescence intensity under different DA concentrations. The physically immobilized bioprobe did not show notable PL quenching within the linear range (0–90 μM) of DA, as shown in Fig. S10 b. We believe that this behavior is

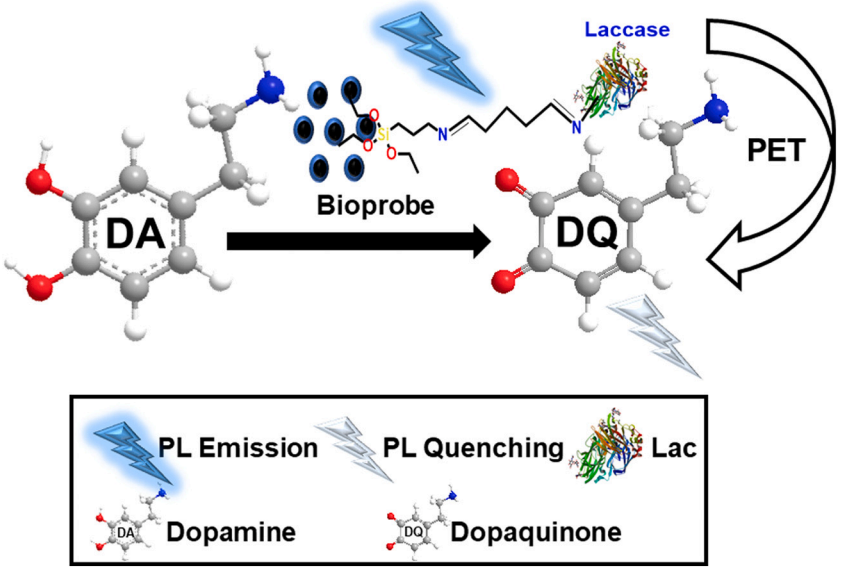

Fig. 9. Schematic representation for the plausible mechanism of PL quenching of bioprobe by DA.

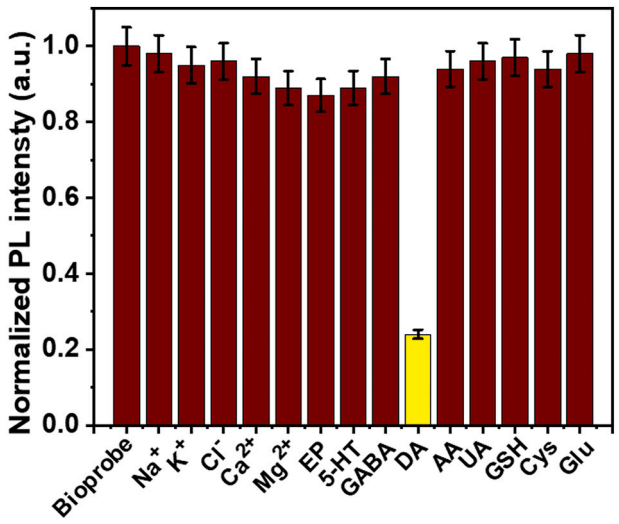

Fig. 10. Selectivity of Bioprobe for DA sensing in the presence of other potential interferants. The concentrations of DA were 30 μM and the other interferants were 90 μM, respectively.

due to improper conjugation between the CDD-CDs and laccase enzyme, i.e. only physical adsorption. In this report, we emphasize the significance of the chemical immobilization of CDD-CDs and laccase enzymes, which was a very important factor for good sensitivity and specificity towards DA. We compared the sensitivity of the chemically immobilized bioprobe with a physical combination of CDD-CDs, APT-CDs, and laccase. For this, CDD-CDs, APT-CDs, and laccase were separately mixed with DA (30 μM), and PL quenching response was measured, as shown in Fig. S11. More importantly, significant fluorescence quenching was showed by the bioprobe while no quenching was noticed with a physical combination of CDD-CDs, APT-CDs, and laccase. It suggests that the chemically immobilized bioprobe is crucial for DA sensing.

3.5. Fluorescence sensing of DA using bioprobe immobilized on a tapered optical fiber

The sensitivity of the immobilized bioprobe on the tapered optical fiber was investigated using various concentrations of DA. Fig. 8 c shows PL quenching of the bioprobe on the fiber by up to 40% upon the addition of DA at various concentrations that ranged from to 0–10 μM. A linear regression curve was plotted between (F_0 – F / F_0) and DA concentrations (0–0.4 μM), which presented an excellent correlation coefficient ($R^2 = 0.994$), as shown in Fig. 8 d. The detection limit for DA was calculated as 46.4 nM. Further, to confirm the importance of tapering for DA sensing, we performed PL measurements in the optical fiber without tapering. In this case, the bioprobe showed rapid PL fluctuations in the presence of DA and did not show a linear quenching tendency against DA concentrations (0.1–0.3 μM), as illustrated in Fig. S12. These results show that tapering of the optical fiber is very important for DA sensing by fluorescence quenching.

3.6. Plausible PL mechanism for DA

The fluorescence of the bioprobe was greatly quenched by the addition of DA, as discussed in the above sections. Fig. 9 shows the plausible PL mechanism for the fluorescence quenching of the bioprobe. When DA is added to the bioprobe, the DA molecule undergoes an oxidation reaction that is facilitated by the laccase enzyme present in the bioprobe. Consequently, DA is converted into DQ (dopaquinone), and photoinduced electron transfer (PET) takes place between the bioprobe and DQ, in which CDD-CDs act as electron donors and DQ as electron acceptors to lead to PL quenching of the bioprobe. For further investigations of the PL quenching mechanism, we performed a time-resolved PL lifetime decay analysis for the bioprobe before and after DA addition, as illustrated in Fig. S13. For this, we employed a double exponential function for fitting, as per the following equation:

$$D(t) = \sum_{i=1}^{n} ai\ exp\left(-\frac{t}{\tau i}\right) \quad (1)$$

where D, τ_i, and a_i represent the PL decay, lifetime, and pre-exponential factors, respectively. The bioprobe showed a lifetime τ_1 of 9.05 ns and lifetime τ_2 of 0.034 ns. After treating the bioprobe with DA, τ_1 decreased to 7.18 ns and τ_2 of 0.032 ns. This was evident for the proposed bioprobe, which offers a plausible PL quenching response in the presence of DA that may be due to the PET process between the bioprobe and DQ [68].

3.7. Selectivity of the bioprobe

The selectivity of the bioprobe towards DA was compared by monitoring the PL intensity variations of the bioprobe with potential interferants, such as metal ions (Na^+, K^+, Cl^-, Ca^{2+}, and Mg^{2+}), contemporary neurotransmitters (epinephrine, serotonin, and GABA), and other amino acids and macromolecules (L-ascorbic acid, uric acid, L-glutathione, cysteine, and glucose), as shown in Fig. 10. For other interferants, a higher concentration (90 μM) was used, while 30 μM DA was used for bioprobe. Almost 80% of PL quenching was observed in the bioprobe with DA, while only slight PL quenching was observed with

Table 1
Comparison of analytical performances of the bioprobe for DA sensing, compared to formerly reported DA sensors.

Type of nanomaterial	Type of sensor	Optical fiber	Linear range	LOD	Ref
Carbon dots/ tyrosinase hybrid	Fluorescence	No	0.21–131.8 μM	60 nM	34
Carbon dots/ tyrosinase conjugate	Fluorescence	No	0.1–6.0 μM	60 nM	35
TGA-capped CdTe QDs/ laccase hybrid	Fluorescence	No	0.3–100 μM	0.16 μM	38
Silver nanoparticles (AgNPs)	SPR	Plastic cladded silica fiber	0.2–30 μM	0.2 μM	43
Graphene layer/ gold (Au) film coated and functionalized with DNA aptamers	SPR	TFBG	10^{-7}–10^{-2} μM	10^{-7} μM	44
Ag film/Nafion/ MWCNTs-PPy MIP	SPR	Plastic cladded silica fiber	10^{-3}–10^{-1} μM	18.9 pM	45
CdSe/ZnS QDs	Fluorescence	MWONS	0–228 μM	100 nM	47
APTES-functionalized and laccase immobilized CDD-CDs (Bioprobe)	Fluorescence	Plastic cladded silica fiber	0–30 μM 0–10 μM	41.2 nM (in PBS buffer) 46.4 nM (in tapered optical fiber)	This work

TGA: thioglycolic acid.
QDs: quantum dots.
SPR: surface plasmon resonance.
TFBG: tilted fiber Bragg grating.
MWCNTs: multiwalled carbon nanotubes.
MWONS: miniaturized and wireless optical neurotransmitter sensing system.
CDD-CDs: curcumin-DMF derived CDs.

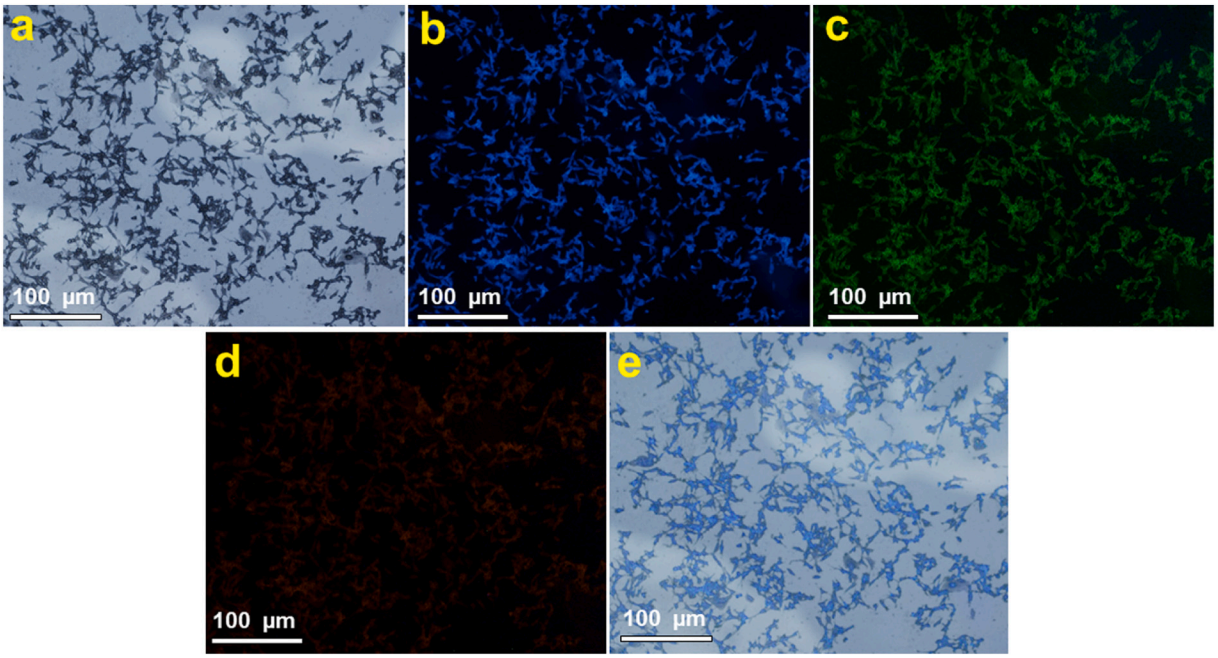

Fig. 11. Fluorescence microscopic images of the SH-SY5Y cells incubated with bioprobe for 3 h. (a) bright field and fluorescence images were taken at excitation wavelengths of (b) 405 nm (blue), (c) 488 nm (green), (d) 543 nm (red) and (e) overlay image. (For interpretation of the references to color in this figure legend, the reader is referred to the web version of this article.)

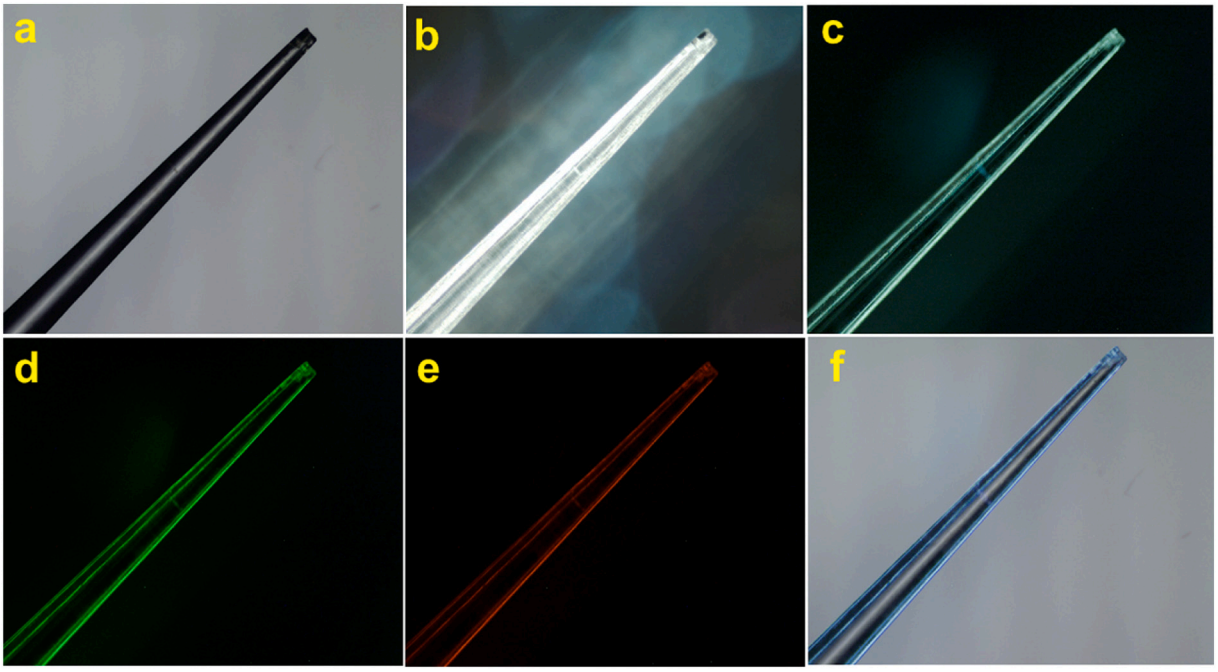

Fig. 12. Fluorescence microscopic images of the tapered optical fiber incubated with immobilized bioprobe for 3 h. (a) bright field, (b) dark filed and fluorescence images were processed at excitation wavelengths of (c) 405 nm (blue), (d) 488 nm (green), (e) 543 nm (red), and (f) overlay image. (For interpretation of the references to color in this figure legend, the reader is referred to the web version of this article.)

other interferants. This suggests that the bioprobe has very high specificity for the detection of DA by fluorescence quenching. Furthermore, the quenching efficiency of the bioprobe was not considerably altered by the presence of interferants. These results emphasize that bioprobes have excellent potential for detecting DA with meritorious sensitivity and selectivity. Table 1 shows a detailed comparison of the current bioprobe and formerly reported sensors for DA sensing. From this study, we believe that our enzyme-based biosensor, i.e. bioprobe, demonstrates superior sensitivity and stability as compared to that reported by other DA sensors. Further, salt effect and stability studies of CDD-CDs and bioprobe are available in supplementary information (Figs. S14–16).

3.8. Bioprobe cytotoxicity studies

The cytotoxicity of the bioprobe was evaluated using MTT assay against SH-SY5Y cells. The bioprobe has exerts moderate cytotoxic

effects after incubating 48 h against SH-SY5Y cells as shown in Fig. S17. The cell viability was gradually decreased with an increase in the bioprobe concentrations. It suggests that bioprobe shows an adequate cytotoxic effect on neuroblastoma cells.

3.9. Multi-color imaging applications of the bioprobe in SH-SY5Y cells and tapered optical fiber

The bioprobe displayed promising fluorescence emission behavior in the SH-SY5Y cells. Fig. 11 a–e show the multi-color imaging of the bioprobe after incubated for 3 h at different excitation wavelengths, such as 405 (blue), 488 (green), and 543 nm (red). It shows that the bioprobe presents excellent uptake in SH-SY5Y cells. On the other hand, the bioprobe after incubating 3 h in the tapered optical fibers demonstrated the multi-color (blue, green, and red) fluorescence imaging behavior (Fig. 12 a–f). We tested the bioprobe after incubated for 3 h in the optical fibers without tapering to explore multi-color imaging studies. Our findings showed a well-organized multi-color imaging response with blue, green, and red fluorescence (Fig. S18 a–f). In total, these studies shed light on the bioimaging performance of the bioprobe for both in vitro (SH-SY5Y) and DA sensing applications.

4. Conclusion

We have successfully synthesized curcumin-based CDs by microwave irradiation and functionalized with APTES and the laccase enzyme was immobilized using the covalent immobilization technique. Further, using a simple dip-coating process, the bioprobe was immobilized on the tapered optical fiber. The as-proposed bioprobe is high on demand for dual sensing of DA in PBS buffer and tapered optical fiber. The bioprobe showed excellent photostability, biocompatibility, and adequate PL stability under high oxidation conditions. It delivered superior multi-color imaging properties in SH-SY5Y cells and optical fiber with blue, green, and red color emissions. The time-resolved PL lifetime decay studies explained the PET process by the bioprobe that is resulted in the DA sensing. In human serum and CSF samples, the practicality of the bioprobe was extensively studied; good recovery values were shown. This work offers an opportunity for other CD-based nanomaterials for immobilizing various enzymes. However, a few main limitations can be addressed for this bioprobe. First is that blue-colored emission is limited for determining DA at cellular and organism levels due to the interference generated from the biological matrix. The other is that the bioprobe is difficult to detect DA in picomolar ranges with ultra-level detection. Thus, long-wavelength emissive bioprobes can be needed in the future for efficient *in vitro* and *in vivo* detection of DA.

CRediT authorship contribution statement

Roopkumar Sangubotla: Conceptualization, Investigation, Methodology, Data curation, Formal analysis, Writing – original draft. **Jongsung Kim:** Supervision, Validation, Funding acquisition, Project administration, Writing – review & editing.

Declaration of competing interest

The authors declare that they have no known competing financial interests or personal relationships that could have appeared to influence the work reported in this paper.

Acknowledgements

We thank the Smart Materials Research Center for IoT at Gachon University for their technical support with instruments (FT-IR, UV–Vis spectroscopy, and SEM). This research was supported by the Basic Science Research Program through the National Research Foundation of Korea (NRF) that is funded by the Ministry of Education (NRF2017R1D1A1B04035070) and by Korea Basic Institute (National Research facilities and Equipment Center) grant that was funded by the Ministry of Education (2020R1A6C103A050).

Appendix A. Supplementary data

All the data related to materials, instrumentation, salt effect and stability studies, quantum yield measurements, and real sample analysis are available in the supplementary information. Supplementary data to this article can be found online at doi:https://doi.org/10.1016/j.msec.2021.111916.

References

[1] R. Sangubotla, J. Kim, Recent trends in analytical approaches for detecting neurotransmitters in Alzheimer's disease, Trends Anal. Chem. 105 (2018) 240–250.
[2] N. Alizadeh, A. Salimi, Polymer dots as a novel probe for fluorescence sensing of dopamine and imaging in single living cell using droplet microfluidic platform, Anal. Chim. Acta 1091 (2019) 40–49.
[3] R. Das, K.K. Paul, P.K. Giri, Highly sensitive and selective label-free detection of dopamine in human serum based on nitrogen-doped graphene quantum dots decorated on au nanoparticles: mechanistic insights through microscopic and spectroscopic studies, Appl. Surf. Sci. 490 (2019) 318–330.
[4] N. Thakur, A. Chaturvedi, D. Mandal, T.C. Nagaiah, Ultrasensitive and highly selective detection of dopamine by a NiFeP based flexible electrochemical sensor, Chem. Commun. 56 (2020) 8448–8451.
[5] Y. Yu, R.P.S. de Campos, S. Hong, D.L. Krastev, S. Sadanand, Y. Leung, A. R. Wheeler, A microfluidic platform for continuous monitoring of dopamine homeostasis in dopaminergic cells, Microsyst. Nanoeng. 5 (2019) 10.
[6] W. Yang, Y. Yu, Y. Tang, K. Li, Z. Zhao, M. Li, G. Yin, H. Li, S. Sun, Enhancing electrochemical detection of dopamine via dumbbell-like FePt-Fe_3O_4 nanoparticles, Nanoscale. 9 (2017) 1022–1027.
[7] C. Liu, F.A. Gomez, Y. Miao, P. Cui, W. Lee, A colorimetric assay system for dopamine using microfluidic paper-based analytical devices, Talanta. 194 (2019) 171–176.
[8] K. Zhang, Y. Liu, Y. Wang, R. Zhang, J. Liu, J. Wei, H. Qian, K. Qian, R. Chen, B. Liu, Quantitative SERS detection of dopamine in cerebrospinal fluid by dual-recognition induced hot spot generation, ACS Appl. Mater. Interfaces 10 (2018) 15388–15394.
[9] S. Mura, R. Ludmerczki, L. Stagi, S. Garroni, C.M. Carbonaro, P.C. Ricci, M. F. Casula, L. Malfatti, P. Innocenzi, Integrating sol-gel and carbon dots chemistry for the fabrication of fluorescent hybrid organic-inorganic films, Sci. Rep. 10 (2020) 4770.
[10] H. Guo, B. You, S. Zhao, Y. Wang, G. Sun, Y. Bai, L. Shi, Full-color tunable photoluminescent carbon dots based on oil/water interfacial synthesis and their applications, RSC Adv. 8 (2018) 24002–24012.
[11] S. Venkateswarlu, S. Govindaraju, R. Sangubotla, J. Kim, M.H. Lee, K. Yun, Biosynthesized highly stable Au/C nanodots: ideal probes for the selective and sensitive detection of Hg^{2+} ions, Nanomaterials. 9 (2019) 245.
[12] T.H. Le, H.J. Lee, J.H. Kim, S.J. Park, Detection of ferric ions and catecholamine neurotransmitters via highly fluorescent heteroatom co-doped carbon dots, Sensors. 20 (2020) 3470.
[13] V. Singh, K.S. Rawat, S. Mishra, T. Baghel, S. Fatima, A.A. John, N. Kalleti, D. Singh, A. Nazir, S.K. Rath, A. Goel, Biocompatible fluorescent carbon quantum dots prepared from beetroot extract for *in vivo* live imaging in *C. elegans* and BALB/c mice, J. Mater. Chem. B. 6 (2018) 3366–3371.
[14] T.T. Bui, S.Y. Park, A carbon dot-hemoglobin complex-based biosensor for cholesterol detection, Green Chem. 18 (2016) 4245–4253.
[15] L. Yue, H. Li, Q. Sun, J. Zhang, X. Luo, F. Wu, X. Zhu, Red-emissive ruthenium-containing carbon dots for bioimaging and photodynamic cancer therapy, ACS Appl. Nano Mater. 3 (2020) 869–876.
[16] H. Yang, Y. Liu, Z. Guo, B. Lei, J. Zhuang, X. Zhang, Z. Liu, C. Hu, Hydrophobic carbon dots with blue dispersed emission and red aggregation-induced emission, Nat. Commun. 10 (2019) 1789.
[17] Y. Zhou, E.M. Zahran, B.A. Quiroga, J. Perez, K.J. Mintz, Z. Peng, P.Y. Liyanage, R. R. Pandey, C.C. Chusuei, R.M. Leblanc, Size-dependent photocatalytic activity of carbon dots with surface-state determined photoluminescence, Appl. Catal. B Environ. 248 (2019) 157–166.
[18] T. Pal, S. Mohiyuddin, G. Packirisamy, Facile and green synthesis of multicolor fluorescence carbon dots from curcumin: *in vitro* and *in vivo* bioimaging and other applications, ACS Omega 3 (2018) 831–843.
[19] S.D. Hettiarachchi, R.M. Graham, K.J. Mintz, Y. Zhou, S. Vanni, Z. Peng, R. M. Leblanc, Triple conjugated carbon dots as a nano-drug delivery model for glioblastoma brain tumors, Nanoscale. 11 (2019) 6192–6205.
[20] B. Wang, J. Li, Z. Tang, B. Yang, S. Lu, Near-infrared emissive carbon dots with 33.96% emission in aqueous solution for cellular sensing and light-emitting diodes, Sci. Bull. 64 (2019) 1285–1292.
[21] B.A. Lakshmi, R. Sangubotla, J. Kim, H.T. Ha, S. Kim, Lanthanum mediated rutin yellow-fluorescent carbon dots as multifaceted sensing probes for the detection of calcium ions in melanoma and plant cells, Mater. Sci. Eng. C 120 (2021), 111644.

[22] B. Wang, J. Yu, L. Sui, S. Zhu, Z. Tang, B. Yang, S. Lu, Rational design of multi-color-emissive carbon dots in a single reaction system by hydrothermal, Adv. Sci. 2001453 (2020).
[23] H. Song, X. Liu, B. Wang, Z. Tang, S. Lu, High production-yield solid-state carbon dots with tunable photoluminescence for white/multi-color light-emitting diodes, Sci. Bull. 64 (2019) 1788–1794.
[24] C.J. Lin, L. Chang, H.W. Chu, H.J. Lin, P.C. Chang, R.Y.L. Wang, B. Unnikrishnan, J.Y. Mao, S.Y. Chen, C.C. Huang, High amplification of the antiviral activity of curcumin through transformation into carbon quantum dots, Small. 15 (2019) 1902641.
[25] J. Gu, X. Li, D. Hu, Y. Liu, G. Zhang, X. Jia, W. Huang, K. Xi, Green synthesis of amphiphilic carbon dots from organic solvents: application in fluorescent polymer composites and bio-imaging, RSC Adv. 8 (2018) 12556–12561.
[26] B. Shao, Z. Liu, G. Zeng, Y. Liu, X. Yang, C. Zhou, M. Chen, Y. Liu, Y. Jiang, M. Yan, Immobilization of laccase on hollow mesoporous carbon nanospheres: noteworthy immobilization, excellent stability and efficacious for antibiotic contaminants removal, J. Hazard. Mater. 362 (2019) 318–326.
[27] J. Zdarta, K. Jankowska, M. Wyszowska, E.K. Gawrońska, A.Z. Grześkowiak, M. Pinelo, A.S. Meyer, D. Moszyński, T. Jesionowski, Robust biodegradation of naproxen and diclofenac by laccase immobilized using electrospun nanofibers with enhanced stability and reusability, Mater. Sci. Eng. C 103 (2019) 109789.
[28] C. Wardak, B.P. Bator, S. Malinowski, Application of cold plasma corona discharge in preparation of laccase-based biosensors for dopamine determination, Mater. Sci. Eng. C. 116 (2020) 111199.
[29] T. Kavetskyy, O. Smutok, O. Demkiv, I. Maťko, H. Švajdlenková, O. Šauša, I. Nováke, D. Berek, K. Čechová, M. Pecz, O.N. Dytso, R.W. Nowak, D. Broda, M. Gonchar, Bożena Zgardzińska, Microporous carbon fibers as electroconductive immobilization matrixes: effect of their structure on operational parameters of laccase-based amperometric biosensor, Mater. Sci. Eng. C 109 (2020) 110570.
[30] S. Palanisamy, S.K. Ramaraj, S.M. Chen, T.C.K. Yang, P.Y. Fan, T.W. Chen, V. Velusamy, S. Selvam, A novel laccase biosensor based on laccase immobilized graphene-cellulose microfiber composite modified screen-printed carbon electrode for sensitive determination of catechol, Sci. Rep. 7 (2017) 41214.
[31] N.A. Samak, Y. Tan, K. Sui, T.T. Xia, K. Wang, C. Guo, C. Liu, CotA laccase immobilized on functionalized magnetic graphene oxide nano-sheets for efficient biocatalysis, Mol. Catal. 445 (2018) 269–278.
[32] W. Zhao, K. Wang, Y. Wei, Y. Ma, L. Liu, X. Huang, laccase biosensor based on phytic acid modification of nanostructured SiO_2 surface for sensitive detection of dopamine, Langmuir. 30 (2014) 11131–11137.
[33] Z. Li, Y. Zheng, T. Gao, Z. Liu, J. Zhang, G. Zhou, Fabrication of biosensor based on core–shell and large void structured magnetic mesoporous microspheres immobilized with laccase for dopamine detection, J. Mater. Sci. 53 (2018) 7996–8008.
[34] T.R. Silva, I.C. Vieira, A biosensor based on gold nanoparticles stabilized in poly (allylamine hydrochloride) and decorated with laccase for determination of dopamine, **Analyst**. **141** 2016 (216–224).
[35] R. Sangubotla, J. Kim, A facile enzymatic approach for selective detection of γ-aminobutyric acid using corn-derived fluorescent carbon dots, Appl. Surf. Sci. 490 (2019) 61–69.
[36] H. Li, J. Liu, M. Yang, W. Kong, H. Huang, Y. Liu, Highly sensitive, stable, and precise detection of dopamine with carbon dots/tyrosinase hybrid as fluorescent probe, RSC Adv. 4 (2014) 46437–46443.
[37] Z. Tang, K. Jiang, S. Sun, S. Qian, Y. Wang, H. Lin, A conjugated carbon-dot–tyrosinase bioprobe for highly selective and sensitive detection of dopamine, Analyst. 144 (2019) 468–473.
[38] M. Shamsipur, M. Shanehasz, K. Khajeh, N. Mollania, S.H. Kazemi, A novel quantum dot–laccase hybrid nanobiosensor for low level determination of dopamine, Analyst. 137 (2012) 5553–5559.
[39] G. Zhu, L. Cheng, R. Qi, M. Zhang, J. Zhao, L. Zhu, M. Dong, A metal-organic zeolitic framework with immobilized urease for use in a tapered optical fiber urea biosensor, Microchim. Acta 187 (2020) 72.
[40] T. Liu, Y. Zhao, Z. Zhang, P. Zhang, J. Li, R. Yang, C. Yang, L. Zhou, A fiber optic biosensor for specific identification of dead *Escherichia coli* O157:H7, Sens. Actuators B Chem. 196 (2014) 161–167.
[41] S.H.K. Yap, K.K. Chan, G. Zhang, S.C. Tjin, K.T. Yong, Carbon dot-functionalized interferometric optical fiber sensor for detection of ferric ions in biological samples, ACS Appl. Mater. Interfaces 11 (2019) 28546–28553.
[42] L.I.B. Silva, F.D.P. Ferreira, A.C. Freitas, T.A.P. Rocha-Santos, A.C. Duarte, Optical fiber biosensor coupled to chromatographic separation for screening of dopamine, norepinephrine and epinephrine in human urine and plasma, Talanta. 80 (2009) 853–857.
[43] D.R. Raj, S. Prasanth, T.V. Vineeshkumar, C. Sudarsanakumar, Surface plasmon resonance based fiber optic dopamine sensor using green synthesized silver nanoparticles, Sens. Actuators B Chem. 224 (2016) 600–606.
[44] W. Hu, Y. Huang, C. Chen, Y. Liu, T. Guo, B.O. Guan, Highly sensitive detection of dopamine using a graphene functionalized plasmonic fiber-optic sensor with aptamer conformational amplification, Sens. Actuators B Chem. 264 (2018) 440–447.
[45] A. Pathak, B.D. Gupta, Ultra-selective fiber optic SPR platform for the sensing of dopamine in synthetic cerebrospinal fluid incorporating permselective nafion membrane and surface imprinted MWCNTs-PPy matrix, Biosens. Bioelectron. 133 (2019) 205–214.
[46] J. Yoo, S.J. Park, J. Kim, Fabrication and characterization of quantum dot-based optical fiber temperature sensor, Mol. Cryst. Liq. Cryst. 519 (2010) 62–68.
[47] M.H. Kim, H. Yoon, S.H. Choi, F. Zhao, J. Kim, K.D. Song, U. Lee, Miniaturized and wireless optical neurotransmitter sensor for real-time monitoring of dopamine in the brain, Sensors. 16 (2016) 1894.
[48] J. Hu, B. Yuan, Y. Zhang, M. Guo, Immobilization of laccase on magnetic silica nanoparticles and its application in the oxidation of guaiacol, a phenolic lignin model compound, RSC Adv. 5 (2015) 99439–99447.
[49] L. Scherino, M. Giaquinto, A. Micco, A. Aliberti, E. Bobeico, V.L. Ferrara, M. Ruvo, A. Ricciardi, A. Cusano, A time-efficient dip coating technique for the deposition of microgels onto the optical fiber tip, Fibers 6 (2018) 72.
[50] S.S. Abbas, G.J. Rees, N.L. Kelly, C.E.J. Dancer, J.V. Hanna, T. McNally, Facile silane functionalization of graphene oxide, Nanoscale. 10 (2018) 16231–16242.
[51] A. Ahmadi, B. Ramezanzadeh, M. Mahdavian, Hybrid silane coating reinforced with silanized graphene oxide nanosheets with improved corrosion protective performance, RSC Adv. 6 (2016) 54102–54112.
[52] T. Yan, W. Zhong, R. Yu, G. Yi, Z. Liu, L. Liu, X. Wang, J. Jiang, Nitrogen-doped fluorescent carbon dots used for the imaging and tracing of different cancer cells, RSC Adv. 9 (2019) 24852–24857.
[53] A. Wang, Y.L. Hou, F. Kang, F. Lyu, Y. Xiong, W.C. Chen, C.S. Lee, Z. Xu, A. L. Rogach, J. Lu, Y.Y. Li, Rare earth-free composites of carbon dots/metal-organic framework as white light-emitting phosphor, J. Mater. Chem. C 7 (2019) 2207–2211.
[54] K. Jiang, L. Zhang, J. Lu, C. Xu, C. Cai, H. Lin, Triple-mode emission of carbon dots: applications for advanced anti-counterfeiting, Angew. Chem. Int. Ed. 55 (2016) 7231–7235.
[55] Y. Li, X. Zhong, A.E. Rider, S.A. Furman, K.K. Ostrikov, Fast, energy-efficient synthesis of luminescent carbon quantum dots, Green Chem. 16 (2014) 2566–2570.
[56] B. Qiao, T.J. Wang, H. Gao, Y. Jin, High density silanization of nano-silica particles using -aminopropyltriethoxysilane (APTES), Appl. Surf. Sci. 351 (2015) 646–654.
[57] P.K. Singh, K. Wani, R.K. Ghanekar, A. Prabhune, S. Ogale, From micron to nano-curcumin by sophorolipid co-processing: highly enhanced bioavailability, fluorescence, and anti-cancer efficacy, RSC Adv. 4 (2014) 60334–60341.
[58] K.S. Aneja, S. Bohm, A.S. Khanna, H.L.M. Bohm, Graphene based anticorrosive coatings for Cr (VI) replacement, Nanoscale. 7 (2015) 17879–17888.
[59] A.V. Tran, K.H Shim, T.T.V. Thi, J.K. Kook, S.S.A. An, S.W. Lee, Targeted and controlled drug delivery by multifunctional mesoporous silica nanoparticles with internal fluorescent conjugates and external polydopamine and graphene oxide layers, Acta Biomater. 74 (2018) 397–413.
[60] S. Kashefi, S.M. Borghei, N.M. Mahmoodi, Covalently immobilized laccase onto graphene oxide nanosheets: preparation, characterization, and biodegradation of azo dyes in colored wastewater, J. Mol. Liq. 276 (2019) 153–162.
[61] Y. Yang, W. Kong, H. Li, J. Liu, M. Yang, H. Huang, Y. Liu, Z. Wang, Z. Wang, T. K. Sham, J. Zhong, C. Wang, Z. Liu, S.T. Lee, Z. Kang, Fluorescent n-doped carbon dots as *in vitro* and *in vivo* nanothermometer, ACS Appl. Mater. Interfaces 7 (2015) 27324–27330.
[62] J.W. Ma, W.J. Lee, J.M. Bae, K.S. Jeong, S.H. Oh, J.H. Kim, S.H. Kim, J.H. Seo, J. P. Ahn, H. Kim, M.H. Cho, Carrier mobility enhancement of tensile strained Si and SiGe nanowires via surface defect engineering, Nano Lett. 15 (2015) 7204–7210.
[63] D.H. Jurcakova, M. Seredych, G.Q. Lu, T.J. Bandosz, Combined effect of nitrogen- and oxygen-containing functional groups of microporous activated carbon on its electrochemical performance in supercapacitors, Adv. Funct. Mater. 19 (2009) 438–447.
[64] X. Teng, C. Ma, C. Ge, M. Yan, J. Yang, Y. Zhang, P.C. Morais, H. Bi, Green synthesis of nitrogen-doped carbon dots from konjac flour with "off–on" fluorescence by Fe^{3+} and L-lysine for bioimaging, J. Mater. Chem. B 2 (2014) 4631–4639.
[65] Y. Zhan, B. Shang, M. Chen, L. Wu, One-step synthesis of silica-coated carbon dots with controllable solid-state fluorescence for white light-emitting diodes, Small. 15 (2019) 1901161.
[66] Y. Dong, H. Pang, H.B. Yang, C. Guo, J. Shao, Y. Chi, C.M. Li, T. Yu, Carbon-based dots co-doped with nitrogen and sulfur for high quantum yield and excitation-independent emission, Angew. Chem. Int. Ed. Eng. 52 (2013) 7800–7804.
[67] J. Shen, T. Zhang, Y. Cai, X. Chen, S. Shang, J. Li, Highly fluorescent N, S-co-doped carbon dots: synthesis and multiple applications, New J. Chem. 41 (2017) 11125–11137.
[68] X. Li, S. Zhang, S.A. Kulinich, Y. Liu, H. Zeng, Engineering surface states of carbon dots to achieve controllable luminescence for solid-luminescent composites and sensitive Be^{2+} detection, Sci. Rep. 4 (2014) 4976.